Journal of Solid State Chemistry 239 (2016) 99–105

Contents lists available at ScienceDirect

Journal of Solid State Chemistry

journal homepage: www.elsevier.com/locate/jssc

Phase separation, orbital ordering and magnetism in $(La_{0.375}Ca_{0.625})MnO_3$

A. Martinelli [a,*], M. Ferretti [a,b], C. Ritter [c]

[a] SPIN-CNR, C.so Perrone 24, 16152 Genova, Italy
[b] Dipartimento di Chimica e Chimica Industriale, Via Dodecaneso 31, 16146 Genova, Italy
[c] Institute Laue, Langevin, 6 rue Jules Horowitz, 38042 Grenoble Cedex 9, France

ARTICLE INFO

Article history:
Received 8 February 2016
Received in revised form
14 April 2016
Accepted 15 April 2016
Available online 19 April 2016

Keywords:
Manganite
Neutron diffraction
Soft modes
Structural transition
Magnetic ordering

ABSTRACT

At 300 K $(La_{0.375}Ca_{0.625})MnO_3$ crystallizes in the orthorhombic *Pnma* space group; on cooling a *Pnma* → *Pnma* structural transition occurs due to charge-orbital ordering within the Mn sub-lattice, producing a superstructure consistent with a Wigner-crystal model with a tripling of the cell parameter *a*. The primary active mode yielding the observed ordered structure corresponds to the irreducible representation labelled Σ_3, with wave vector (⅓,0,0). Nevertheless, the disordered polymorph stable at room temperature is retained at low temperature as a secondary phase, coexisting with the charge-orbital ordered structure. These two phases display different spin orderings; the antiferromagnetic structure associated to the charge-orbital ordered phase is characterized by a magnetic propagation wave vector **k**=(0,0,½), with a canted spin ordering in the *ac* plane, whereas a C_y-type arrangement develops within the disordered polymorph.

Published by Elsevier Inc.

1. Introduction

The $(La_{1-x}Ca_x)MnO_3$ system exhibits extremely varied and fascinating structural and magnetic properties [1,2]. In particular the Ca-rich (hole doped) compositions are characterized by ordering phenomena resulting from a delicate interplay among charge, lattice and spin degrees of freedom. In fact the substitution of Ca^{2+} with La^{3+} promotes the formation of the Jahn-Teller species Mn^{3+}; as a result below the charge ordering temperature (T_{CO}) electronic carriers become localized onto specific sites of the Mn sub-lattice. The Jahn-Teller effect associated with the Mn^{3+} ions then induces also cooperative lattice distortion due to orbital ordering. As a consequence of both charge and orbital orderings, the magnetic exchange interactions between neighbouring Mn ions become strongly anisotropic and complex magnetic orderings can occur.

Several neutron powder diffraction investigations have been carried for compositions with $0.60 \le x \le 0.67$. For $x=0.60$ a phase separation taking place at low temperature, accompanied by the coexistence of two different magnetic structures, was argued [3]. With the increase of the Ca content up to $x=0.63$ and 0.69, different magnetic reflections were observed, that were related to magnetic propagation vectors **k**=(⅓,0,½) and **k**=(0,0,½) [3]. In-depth investigations revealed that $(La_{0.333}Ca_{0.667})MnO_3$ crystallizes at room temperature in the orthorhombic *Pnma* space group, but below ~ 260 K orbital ordering occurs, inducing a tripling of the *a* axis parameter and a superstructure consistent with a Wigner-crystal model [4,5]; Mn magnetic moments order below 170 K according to an antiferromagnetic structure [4], with a propagation vector **k**=(0,0,½) [5]. For the $(La_{0.35}Ca_{0.65})MnO_3$ compound orbital ordering was detected below 275 K, whereas the onset of magnetic peaks below 160 ± 3 K, but the magnetic structure was not analyzed in detail [6]. For samples with $0.63 \le x \le 0.67$, superlattice reflections were detected below $T_{CO}=260$ K by transmission electron microscopy (TEM); in particular a modulation wave vector **q**=(~⅓,0,0) was observed below T_{CO} [7]. Further TEM analyses at low temperature on a sample with composition $(La_{0.33}Ca_{0.67})MnO_3$ corroborated the Wigner-crystal structural model, confirming the occurrence of a modulation wave vector **q**=(~⅓,0,0) [8].

In this paper we investigate the structural and magnetic ordering properties of the $(La_{0.375}Ca_{0.625})MnO_3$ composition, as obtained from accurate neutron powder diffraction analysis carried out between 300 and 5 K.

2. Experimental

A polycrystalline sample with nominal composition $(La_{0.375}Ca_{0.625})MnO_3$ was prepared by means of a solid state reaction among

* Corresponding author.
E-mail address: alberto.martinelli@spin.cnr.it (A. Martinelli).

http://dx.doi.org/10.1016/j.jssc.2016.04.023
0022-4596/Published by Elsevier Inc.

stoichiometric amount of binary oxides (CaO 99.95% Aldrich; La_2O_3 99.99% Alfa Aesar; MnO_2 99.999% Alfa Aesar). Four thermal treatments with intermediate grinding were carried out, the first at 1523 K for 15 h and the remaining at 1603 K for 18 h. Neutron powder diffraction (NPD) analysis was carried out at the Institute Laue Langevin using the D1A high resolution diffractometer; NPD patterns were collected at selected temperatures between 5 and 300 K using a wavelength of $\lambda = 1.91$ Å. The crystal and magnetic structures were refined using the program Fullprof [9]. By means of representation analysis [10], possible spin orderings were evaluated, using the programs BasIreps [11,12] contained in the Fullprof suite and SARAh [13]. By means of a $Na_2Ca_3Al_2F_{14}$ (NAC) standard an instrumental resolution file was obtained and used in the refinements in order to detect micro-structural contributions to the NPD peak shape. The diffraction lines were modelled by a Thompson-Cox-Hastings pseudo-Voigt convoluted with axial divergence asymmetry function and the background by a fifth-order polynomial. The following parameters were refined in the final refinement cycle: the overall scale factor; the background (five parameters of the 5th order polynomial); 2θ-Zero; the unit cell parameters; the specimen displacement; the reflection-profile asymmetry; Wyckoff positions not constrained by symmetry; the isotropic thermal parameters *B*; the anisotropic strain parameters; the Fourier coefficients of the magnetic structure.

3. Results and discussion

3.1. Crystal structure of $(La_{0.375}Ca_{0.625})MnO_3$

At 300 K $(La_{0.375}Ca_{0.625})MnO_3$ crystallizes in the orthorhombic *Pnma* space group (structural data are reported in Table 1). Rietveld refinement of the site occupancy parameters do not evidence significant deviations from the nominal composition. The evolution of the lattice parameters on cooling (Fig. 1) reveals the occurrence of charge and orbital orderings; in fact below the ordering temperature the *b* axis rapidly decreases, whereas the *a* and *c* axes increase, in agreement to what observed in $(La_{0.33}Ca_{0.67})MnO_3$) [4,5]. Unfortunately, our high-resolution neutron diffraction data lack enough intensity to distinguish superlattice reflections accompanying the structural ordering. Charge and orbital orderings can be represented using a structural model similar to that developed for the so called Wigner-crystal model of $(La_{0.333}Ca_{0.667})MnO_3$ and in agreement with the lattice ordering detected by electron diffraction [5,7,8]. As a result a *Pnma* → *Pnma* structural transition takes place, producing a tripling of the cell parameter *a* and the splitting of all the Wyckoff orbits, increasing the number of independent atoms from 4 to 11 (Tables 1 and 2). Despite the substantial deviation of the $[Mn^{3+}]/[Mn^{4+}]$ ratio from the optimal value, the tendency towards charge and orbital ordering in $(La_{0.375}Ca_{0.625})MnO_3$ is dominating, as evidenced by the

Table 1
Structural data of $(La_{0.375}Ca_{0.625})MnO_3$ at 300 K (from Rietveld refinement of NPD data).

Space group	*Pnma* (62)				
Lattice parameters (Å)	*a*		*b*	*c*	
	5.3956(1)		7.5866(1)	5.4037(1)	
Atom	Wyckoff site	*x*	*y*	*z*	
La/Ca(1)	4*c*	0.0195(5)	¼	0.9975(7)	
Mn(1)	4*b*	0	0	½	
O(1)	4*c*	0.9918(6)	¼	0.4410(5)	
O(2)	8*d*	0.7206(4)	0.9690(2)	0.2764(5)	
Agreement factors (%)	χ^2	R_{wp}	R_{Bragg}	R_F	
	2.87	5.44	4.38	3.17	

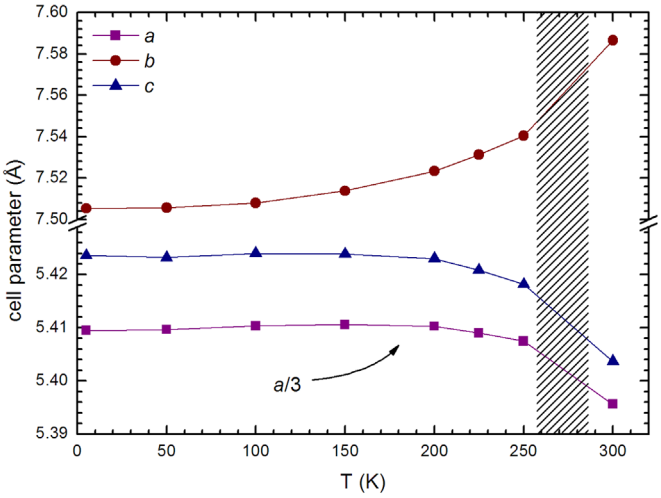

Fig. 1. Evolution of the cell parameters in $(La_{0.375}Ca_{0.625})MnO_3$ on cooling; the hatched area indicates the *T* range inside which orbital ordering occurs.

Table 2
Structural data and agreement factors for the charge-orbital ordered polymorph of $(La_{0.375}Ca_{0.625})MnO_3$ at 5 K (from Rietveld refinement of NPD data).

Space group	*Pnma* (62)				
Lattice parameters (Å)	*a*		*b*	*c*	
	16.2291(1)		7.5056(1)	5.4236(1)	
Atom	Wyckoff site	*x*	*y*	*z*	
La/Ca(1)	4*c*	0.0037(1)	¼	0.9868(3)	
La/Ca(2)	4*c*	0.1577(1)	¾	0.5172(2)	
La/Ca(3)	4*c*	0.1759(1)	¼	0.5186(3)	
Mn(1)	4*b*	0	0	½	
Mn(2)	8*d*	0.1682(1)	0.4985(2)	0.0174(3)	
O(1)	4*c*	0.3327(1)	¼	0.4528(2)	
O(2)	4*c*	0.1591(1)	¼	0.0793(3)	
O(3)	4*c*	0.9996(1)	¾	0.5645(3)	
O(4)	8*d*	0.2404(1)	0.5345(2)	0.2948(2)	
O(5)	8*d*	0.0759(1)	0.9636(1)	0.2287(2)	
O(6)	8*d*	0.0925(1)	0.0274(1)	0.7389(2)	
Agreement factors (%)	χ^2	R_{wp}	R_{Bragg}	R_F	$R_{magnetic}$
	3.04	5.65	3.78	3.47	9.49

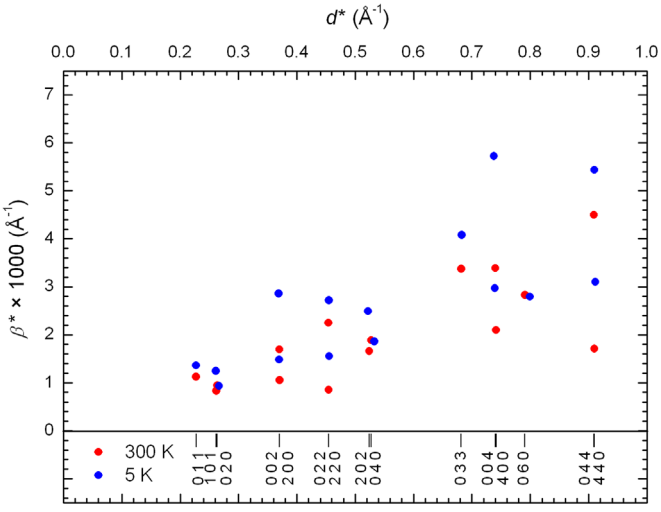

Fig. 2. Superposition of the Williamson-Hall plots obtained from NPD data collected at 300 K and 10 K (data from selected families of crystallographic planes with different orders); in the lower field the corresponding indexed Bragg peaks are listed.

marked cooperative Jahn-Teller distortion characterizing octahedra centred by Mn^{3+} ions located at the 4*b* site.

The microstructural evolution as a function of temperature was investigated by refining the anisotropic strain parameters and analyzing the broadening of diffraction lines by means of the Williamson-Hall plot method [14]. Initially, Rietveld refinements were carried out adopting the structural model of the only disordered polymorph in the whole thermal range; remarkably, very good fits are obtained (at 5 K, R_{Bragg}=5.88%). As a result, size effects are negligible and a straight line passing through the origin and all the points of the different orders of the same reflection is obtained, whose slope provides the microstrain contribution. The superposition of the Williamson-Hall plots obtained using the NPD data collected at 300 K and 5 K clearly reveals that most of the diffraction lines are broadened at low temperature (Fig. 2).

Fig. 3 shows the thermal dependence of the anisotropic microstrain-like contribution to line broadening as calculated using the single disordered phase model. In particular, as the temperature is decreased around the ordering temperature, the microstrain-like broadening increases; further cooling relieves broadening along [0*k*0], but not along [*h*00] and [00*l*]. The observed behaviour suggests that phase-separation takes place on cooling, a scenario corroborated by the analysis of the magnetic

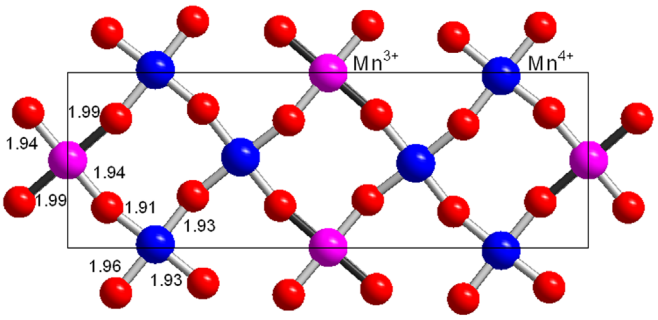

Fig. 5. Arrangement of Mn-O bonds in the *ac* plane of the charge-orbital ordered structure of $(La_{0.375}Ca_{0.625})MnO_3$ viewed along [010]; bond lengths are also reported (Å). Darker sticks represent Mn^{3+}-O bonds elongated due to the cooperative Jahn-Teller distortion.

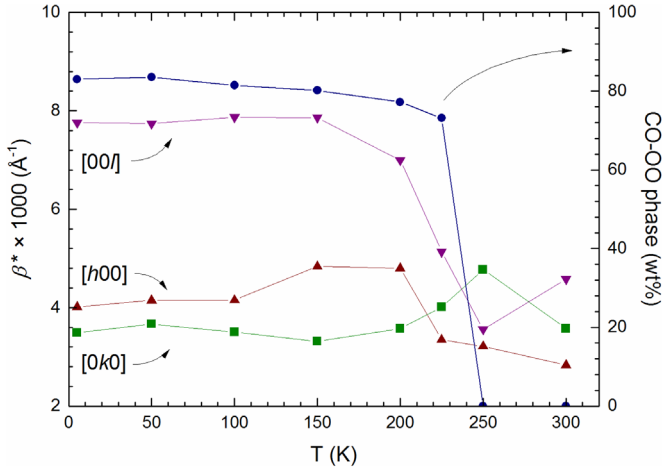

Fig. 3. The evolution on cooling of the microstrain-like line broadening in $(La_{0.375}Ca_{0.625})MnO_3$ along the three main crystallographic directions is compared with the thermal dependence of the charge-orbital ordered (CO-OO) phase fraction.

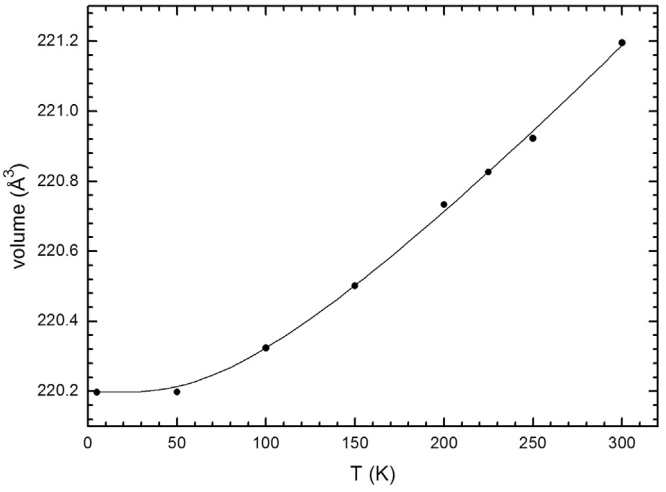

Fig. 6. Thermal dependence of the primitive cell volume in $(La_{0.375}Ca_{0.625})MnO_3$; the solid line shows the best fit to a 2nd order Grüneisen approximation.

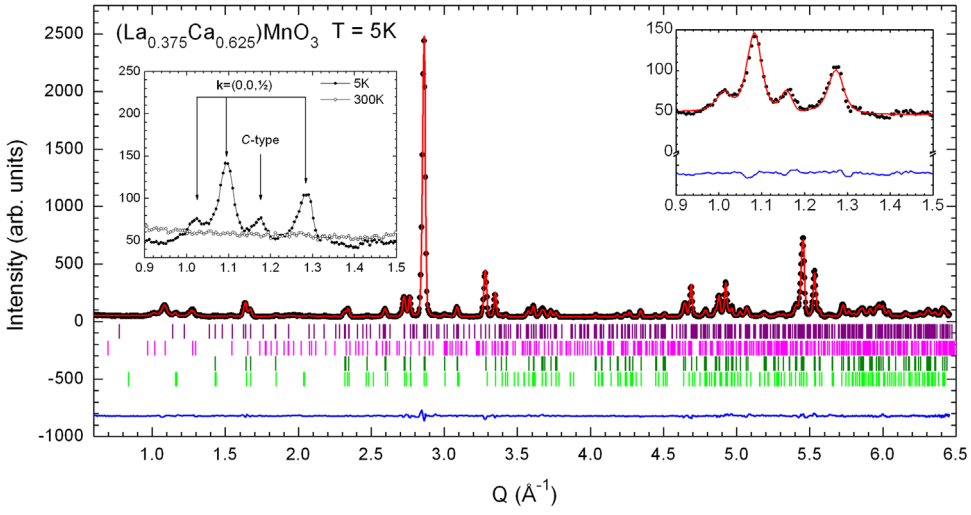

Fig. 4. Rietveld refinement plot for $(La_{0.375}Ca_{0.625})MnO_3$ (NPD data collected at 5 K). In the upper field the continuous red line is the calculated fit superposed to the experimental intensity data; the blue line in the lower field is the difference curve; from the top, the vertical bars indicate Bragg reflections for the charge-orbital ordered phase (purple; crystallographic and magnetic) and the disordered polymorph (green; crystallographic and magnetic). The insets show an enlarged view of the refinement plot in the Q range where main magnetic peaks occur (on the right) and a superposition of the data collected at 300 K and 5 K in the same Q range, evidencing the onset of the magnetic peaks at lower temperature (on the left).(For interpretation of the references to color in this figure legend, the reader is referred to the web version of this article.)

structure (see Section 3.2). On this basis a structural model foreseeing the coexistence of a charge-orbital-ordered phase with a disordered structure was successfully tested; as a result the goodness of fit is improved and the volume fraction of the disordered phase is almost 17%. Due to its paucity and the strong peaks overlapping, only the cell parameters of this secondary phase were refined. For comparison, Fig. 3 shows also the temperature evolution of the charge-orbital ordered phase fraction, as obtained from the two nuclear (disorder+charge−orbital ordered) phases model. It is evident that the marked increase of the microstrain-like contribution to line broadening is strictly connected with the development of the charge-orbital ordered phase.

Fig. 4 shows the corresponding Rietveld refinement plot obtained with NPD data collected at 5 K, whereas structural data are reported in Table 2. Fig. 5 shows a projection of the arrangement of Mn-O_{eq} bonds along [010]; a clear cooperative Jahn-Teller distortion is active, suggesting that Mn^{3+} ions are mainly located at the 4*b* site. As a rule, the valence at each site can be evaluated by means of the bond valence sum (BVS) analysis [15,16] and using the inter-atomic distances obtained from the refined structural data; nonetheless the bond valence parameters are determined at 300 K and corrections would be needed at other temperatures. In addition the occurrence of lattice strains, the possible mixed valence at both Mn sites and the distortion affecting the octahedral Mn^{3+} environment due to the Jahn-Teller effect further reduces the precision of the calculation at the 4*b* site. For BVS calculations a charge ordered scenario were assumed, where the 4*b* site is completely occupied by Mn^{3+} ions whereas Mn^{4+} ions are located at the 8*d* site together with the remaining Mn^{3+} ions. As a result the BVS values are 3.37 v.u. and 3.78 v.u, respectively, corroborating the charge ordered model; by assuming a random distribution of both cationic species the BVS values result 3.49 v.u. and 3.71 v.u, respectively, still in agreement with a tendency towards charge splitting.

The primitive cell volume undergoes no discontinuity at the structural transition. In order to investigate in detail the thermal expansion behaviour of $(La_{0.375}Ca_{0.625})MnO_3$, its cell volume has been fitted between 5 and 300 K, using a Grüneisen 2nd order approximation for the zero-pressure equation of state [17]:

$$V(T) = \frac{V_0 U}{Q - bU} + V_0 \quad (1)$$

where $Q=V_0K_0/\gamma'$ and $b=(K_0'-1)/2$; γ' is a dimensionless Grüneisen parameter of the order of unity; K_0 is the compressibility and K_0' its derivative with respect to applied pressure; V_0 is the zero temperature limit of the unit cell volume; U is the internal energy calculated by the Debye approximation:

$$U(T) = 9Nk_BT\left(\frac{T}{\Theta_D}\right)^3 \int_0^{\frac{T}{\Theta_D}} \frac{x^3 dx}{e^x - 1} \quad (2)$$

where N is the number of atoms in the unit cell; k_B is the Boltzmann's constant; Θ_D is the Debye temperature. The compressibility of $CaMnO_3$ and $LaMnO_3$ are 147 GPa and 141 GPa, respectively,

Table 3
Summary of the basis modes involved in the ordering of $(La_{0.375}Ca_{0.625})MnO_3$.

Atoms	Wyckoff site	Modes
O(2)	8*d*	$\Gamma_1^+(3)$ $\Sigma_3(6)$
O(1), La/Ca(1)	4*c*	$\Gamma_1^+(2)$ $\Sigma_3(4)$
Mn(1)	4*b*	

Table 4
Summary of the mode decomposition of $(La_{0.375}Ca_{0.625})MnO_3$, reporting the amplitudes of all the intervening *irrep* components; data of the low temperature structure from NPD data collected at 150 K.

k vector	*irrep*	Direction	Isotropy sub-group	Dimension	Amplitude (Å)
(0,0,0)	Γ_1^+	(a)	*Pnma* (62)	7	0.119(1)
(⅓,0,0)	Σ_3	(a,0)	*Pnma* (62)	17	0.657(4)

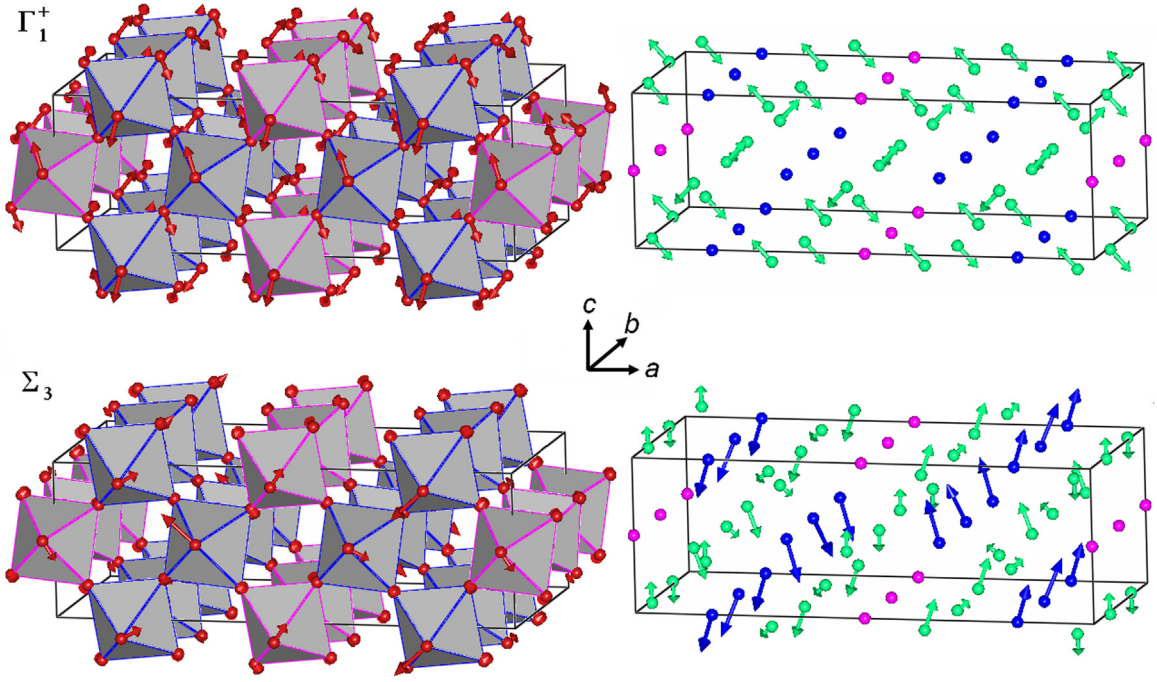

Fig. 7. Atomic displacements in $(La_{0.375}Ca_{0.625})MnO_3$, corresponding to the Γ_1^+ and modes; the description of the distortions affecting the Ca/La (green) and Mn (Mn^{3+}: purple; Mn^{4+}: blue) sub-lattices are evidenced on the right. Arrows show the directions of atomic displacements; for clarity the amplitude of the distortion has been arbitrarily increased. (For interpretation of the references to color in this figure legend, the reader is referred to the web version of this article.)

which are the experimental bulk modulus values extracted from high pressure X-ray powder diffraction measurements [18]. The fitting was carried out assuming these K_0 values and leaving γ', Θ_D and K_0' as free parameters. Fig. 6 shows the resulting fitting curve; Θ_D value turns out to be ~315 K, in fair agreement with the value calculated from heat capacity data for $LaMnO_3$ (Θ_D ~300 K) and $(La_{0.80}Ca_{0.20})MnO_3$ (Θ_D ~390 K) [19,20]. It can be seen that the Grüneisen law well accounts for the observed temperature dependence of the volume in the whole temperature range explored by the experiment.

In order to investigate in detail the ordering transition, the modes involved in the symmetry-breaking distortion were analyzed and their amplitudes calculated. Mode decomposition of the high temperature structure was carried using Amplimode [21]. The primary active mode yielding the observed ordered structure corresponds to the irreducible representation (*irrep*) labelled Σ_3, with wave vector (⅓,0,0) responsible for the tripling of the *a* axis; a secondary *irrep* Γ_1^+ is also active, maintaining the parent lattice symmetry (Table 3). There are 7 modes of symmetry Γ_1^+ and 17 modes of symmetry Σ_3; the primary mode Σ_3 involves all the atoms.

Results obtained by Rietveld refinement using the symmetry mode options are summarized in Table 4; the data of the low temperature structure were obtained from the refinement of the NPD data collected at 150 K, where structural orderings are practically completed (see Fig. 1), but magnetic scattering contribution is almost negligible. Both *irreps* contribute to the structural distortion, the primary mode Σ_3 being characterized by the largest amplitude; their absolute amplitudes are the components of the global structural distortion, amounting to 0.668 Å at 150 K and corresponding to the square root of the sum of the square of the amplitudes listed in the Table 4 for all *irreps*.

Fig. 7 shows the atomic displacements corresponding to the Σ_3 and Γ_1^+ modes; the displacement pattern of La/Ca and Mn atoms resembles that obtained for the Wigner-crystal structure of $(La_{0.333}Ca_{0.667})MnO_3$ [5], but some differences are evident. In particular in $(La_{0.375}Ca_{0.625})MnO_3$ the displacements of the La/Ca and Mn atoms are not always coupled and have a significant secondary component along the *a* axis, whereas in $(La_{0.333}Ca_{0.667})MnO_3$ displacements are coupled and predominantly along the *c* axis. Table 5 lists the amplitude of the global displacements *u* (Σ_3 plus Γ_1^+ mode displacements) relating the disordered and ordered structures.

Ultimately, symmetry breaking can be thus understood in terms of octahedral tilting, cooperative Jahn-Teller distortions and charge-orbital ordering: the Σ_3 mode describes the Jahn-Teller ordering scheme, whereas octahedral tilting depends on the combination of the Σ_3 and Γ_1^+ modes.

Fig. 8 shows the thermal dependences of both modes; the orbital ordering temperature can be safely assumed very similar to that measured for the neighbouring composition $(La_{0.35}Ca_{0.65})MnO_3$ (~275 K) [6]. The amplitude of the primary mode Σ_3 can be identified with the Landau order parameter (η) connecting the two polymorphs; its evolution with temperature is discontinuous, consistent with a 1st order nature of the structural transition, as in $(La_{0.333}Ca_{0.667})MnO_3$ [4]. In the simplest case of a 1 component order parameter associated with the Landau free energy expansion, $F(\eta)$, the following relationship holds [22]:

$$F(\eta) = \frac{[\alpha(T - T_{CO})]}{2}\eta^2 + \frac{\beta}{4}\eta^4 + \frac{\gamma}{6}\eta^6 \quad (3)$$

Which describes a 1st order transition when $\beta < 0$ and $\gamma > 0$. The thermal dependence of the order parameter η then corresponds to:

$$\eta = \pm \{\frac{-\beta + \beta^2 - 4\gamma\cdot[\alpha(T - T_{CO})]^{\frac{1}{2}}}{2\gamma}\}^{\frac{1}{2}} \quad (4)$$

Table 5
Global atomic displacements in $(La_{0.375}Ca_{0.625})MnO_3$: u_x, u_y u_z are in relative units and |*d*| is the absolute distance; data of the low temperature structure from NPD data collected at 150 K.

Atom	Wyckoff site	Atomic distances			
		u_x	u_y	u_z	|*d*| (Å)
La/Ca(1)	4*c*	0.0011	0.0000	−0.0006	0.0177
La/Ca(2)	4*c*	0.0014	0.0000	−0.0006	0.0227
La/Ca(3)	4*c*	0.0022	0.0000	0.0006	0.0359
Mn(1)	4*b*	0.0000	0.0000	0.0000	0.0000
Mn(2)	8*d*	−0.0034	0.0060	−0.0246	0.1511
O(1)	4*c*	−0.0046	0.0000	0.0115	0.0971
O(2)	4*c*	−0.0070	0.0000	−0.0151	0.1396
O(3)	4*c*	−0.0029	0.0000	0.0053	0.0556
O(4)	8*d*	0.0011	−0.0019	−0.0105	0.0613
O(5)	8*d*	0.0008	−0.0037	0.0058	0.0443
O(6)	8*d*	0.0007	0.0061	0.0038	0.0518

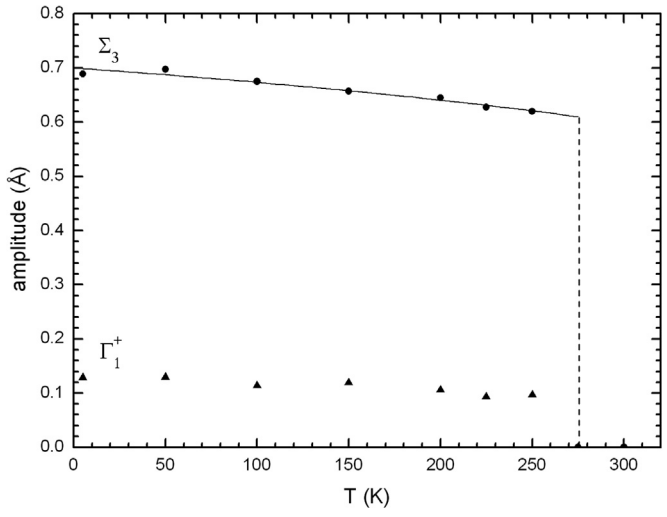

Fig. 8. Thermal dependence of the amplitudes of the primary (Σ_3) and secondary (Γ_1^+) distortions in $(La_{0.375}Ca_{0.625})MnO_3$; the solid line represents the Landau fit for a 1st order transition.

Table 6
Small irreducible representations of the little group $\mathbf{G_k}$=*Pnma*.

Irrep	**Symmetry operators**															
	{1|0,0,0}		{2_z|0,0,½}		{2_y|0,½,0}		{2_x|½,½,½}		{−1|0,0,0}		{m_z|½,0,½}		{m_y|0,½,0}		{m_x|½,½,½}	
Γ_1	1	0	α	0	0	1	0	α	0	−1	0	−α	−1	0	−α	0
	0	1	0	−α	1	0	−α	0	−1	0	α	0	0	−1	0	α
Γ_2	1	0	α	0	0	1	0	α	0	1	0	α	1	0	α	0
	0	1	0	−α	1	0	−α	0	1	0	−α	0	0	1	0	−α

where α, β and γ are refinable parameters; by assuming T_{CO}=270 K, Eq. (2) nicely fits our experimental data (Fig. 8). Remarkably, the η parameter (*i.e.* the amplitudes of the primary Σ_3 distortions) exhibits very little thermal change between 250 K and 5 K, indicating that the 1st order transition is close to the'frozen' limit, a feature observed in other charge ordering transitions, such as in Fe_3O_4 [23].

3.2. Magnetic structure of $(La_{0.375}Ca_{0.625})MnO_3$

At 150 K neutron magnetic scattering is observed, developing into well shaped peaks at lower temperature (Fig. 4, left inset); this result is consistent with what observed for the neighbouring composition with x=0.65 and 0.66, where the onset of magnetic scattering was observed below 160–170 K [4,6]. Remarkably magnetic Bragg peaks display a marked broadening and the refinement of the corresponding size parameter is needed; as a result the average linear size of the coherent magnetic domains is ~15 Å. For $(La_{0.333}Ca_{0.667})MnO_3$ Radaelli et al. [5] reported that the magnetic peak at 1.17 $Å^{-1}$ (see left inset of Fig. 4) belongs to a separate magnetic phase, being consistent with the so called *C*-type spin ordering. The occurrence of this secondary spin ordering can be related to the retention of the disordered polymorph on cooling, supporting the phase-separation previously illustrated (see Section 3.1).

On this basis, the main magnetic Bragg peaks can be successfully indexed according to the propagation vectors $\mathbf{k}$=(0,0,½). By means of the representation analysis of magnetic structures [10], the allowed magnetic moments orderings were calculated, taking into account that in the charge ordered phase of $(La_{0.375}Ca_{0.625})MnO_3$ the magnetic Mn atoms are located at the two different sites 4*b* and 8*d* (see Table 2). As a result, the symmetry analysis using the representation theory provides the little group $\mathbf{G_k}$=*Pnma*. Table 6 lists the irreps of $\mathbf{G_k}$, being complex and of dimension 2, with phase factors $\alpha = exp\{\frac{1}{2}\pi i\}$ and $-\alpha = exp\{\frac{3}{2}\pi i\}$. Γ_m has the characters: $\chi(\Gamma_m - 4b)$=(12,0,0,0,0,0,0,0) and $\chi(\Gamma_m - 8d)$=(24,0,0,0,0,0,0,0) and decomposes in terms of irreps as $\Gamma_m(4b)=3\,\Gamma_1 \oplus 3\,\Gamma_2$ and $\Gamma_m(8d)=6\,\Gamma_1 \oplus 6\,\Gamma_2$. The Fourier coefficients are real, since $\mathbf{k}$ is equivalent to $-\mathbf{k}$.

Experimentally a good fit has been obtained by applying the representation Γ_1 for $\mathbf{G_k}$ (at both 4*b* and 8*d*). The inset of Fig. 4 (on the right) shows an enlarged view of the Rietveld refinement plot, in the region where magnetic neutron scattering is more intense, whereas Table 7 lists the refined magnetic moments. Remarkably, the magnitude of the magnetic moment at the 4*b* site (3.8 μ_B) agrees fairly well with the value predicted for Mn^{3+}(4.0 μ_B), corroborating the charge ordering scenario; conversely the total magnetic moment at the 8*d* site (2.4 μ_B) results significantly reduced than expected (~3.1 μ_B), suggesting the occurrence of some degree of magnetic frustration. The magnetic structure is schematically represented in Fig. 9: in a quite good agreement with the spin arrangement reported by Radaelli et al. [5] and Fernández-Diaz et al. [4] for $(La_{0.333}Ca_{0.667})MnO_3$, a canted spin order occurs, with magnetic moments lying in the *ac* plane and with magnetic moments of Mn^{3+}ions parallel to the elongated Mn-O bonds (see Fig. 5).

The basis vectors associated to the 4*b* and 8*d* sites in the charge-orbital ordered polymorph of $(La_{0.375}Ca_{0.625})MnO_3$ belong to a same irrep, indicating that inter-site interactions are dominant. The same situation could indeed arise in the case that the intra-site coupling of one site would be dominant and a strong inter-site coupling would lead to the polarisation of the second magnetic site. However, in this case one would expect the presence of two distinct magnetic phase transitions; this was not observed in the similar compound $(La_{0.35}Ca_{0.65})MnO_3$ [6].

Table 7
Refined magnetic moments for the magnetic structure of $(La_{0.375}Ca_{0.625})MnO_3$ at 5 K.

Wyckoff site	Coordinates	μ_x (μ_B)	μ_y (μ_B)	μ_z (μ_B)	μ_{Tot} (μ_B)
4*b*	0,0,½	−2.4(1)	0	−2.9(2)	3.8(2)
	½,0,0	2.4(1)	0	−2.9(2)	
	0,½,½	2.4(1)	0	2.9(2)	
	½,½,0	−2.4(1)	0	2.9(2)	
8*d*	0.168,0.498,00.017	2.4(1)	0	−0.3(1)	2.4(1)
	0.668,0.002,00.483	2.4(1)	0	0.3(1)	
	0.332,0.502,00.517	−2.4(1)	0	−0.3(1)	
	0.832,0.998,00.983	−2.4(1)	0	0.3(1)	
	0.832,0.502,00.983	2.4(1)	0	−0.3(1)	
	0.668,0.498,00.483	−2.4(1)	0	−0.3(1)	
	0.168,0.002,00.017	−2.4(1)	0	0.3(1)	
	0.332,0.998,00.517	2.4(1)	0	0.3(1)	

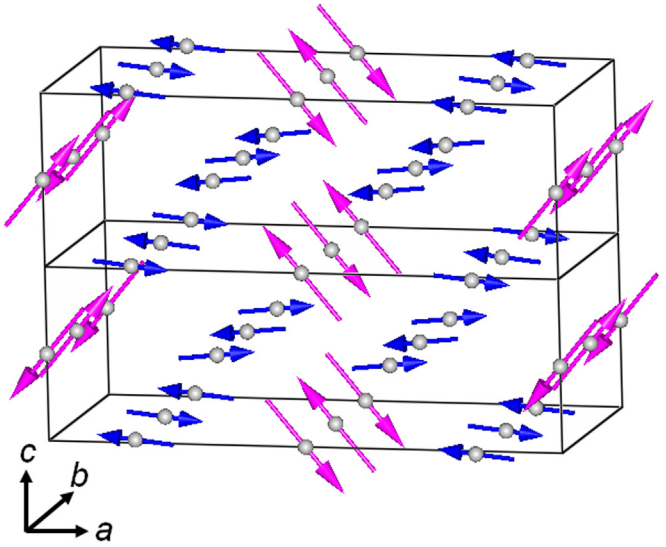

Fig. 9. Schematic representation of the magnetic structure of $(La_{0.375}Ca_{0.625})MnO_3$ at 5 K (Mn^{3+}moments: magenta arrows; Mn^{4+}moments: blue arrows).(For interpretation of the references to color in this figure legend, the reader is referred to the web version of this article.)

As afore mentioned, a secondary *C*-type spin ordering associated to the disordered polymorph is also present. The limited intensity and number of Bragg peaks do not allow to firmly determine the orientation of the magnetic moments. Nonetheless, in a previous investigation [24], we ascertained that a C_y-type structure takes place below ~175 K within the strained regions of $(La_{1-x}Ca_x)MnO_3$ nanoparticles with x=0.50 and 0.75. By using this magnetic structural model the C_y-type ordering is refined with an ordered magnetic moment of ~ 0.72(4) μ_B and $R_{magnetic}$=11.5%. In this context it is worth to note that Ca and La ions (as well as their associated charges) are not perfectly arranged in the lattice; this uneven distribution can determine conditions favouring charge ordering in the largest fraction of the lattice, but also significant local deviations from a perfect random distribution. In this latter case the local increase of Ca^{2+}or La^{3+}content can be detrimental for charge ordering and thus the disordered structure can be retained at low temperature. This secondary phase is intimately admixed with the ordered polymorph, where a notable change of the cell parameters occurs, driven by orbital ordering. In this way the disordered phase can experience a strong lattice strain at low temperature, favouring the C_y-type spin ordering.

4. Conclusions

Neutron powder diffraction analysis was carried out in order to analyze the evolution of the structural and magnetic properties of $(La_{0.375}Ca_{0.625})MnO_3$ between 5 and 300 K. On cooling a *Pnma* → *Pnma* structural transition takes place on account of charge and orbital ordering within the Mn sub-lattice; this symmetry breaking is driven by the primary mode Σ_3, characterized by a wave vector (⅓,0,0), thus producing a tripling of the cell parameter *a* in the ordered structure. The variation of the Landau order parameter is consistent with a 1st order nature of the structural transition. The primitive cell volume undergoes no discontinuity at the structural transition and follows a Grüneisen 2nd order approximation for the zero-pressure equation of state, from which a Debye temperature of ~315 K results. At lower temperature antiferromagnetic ordering takes place: the magnetic structure is characterized by a propagation vectors $\mathbf{k}=(0,0,½)$ and a canted spin arrangement in the *ac* plane. A significant percentage of the sample retains the disordered structure at low temperature, coexisting with the ordered polymorph; in this secondary phase a C_y-type spin ordering takes place.

References

[1] E.O. Wollan, W.C. Koehler, Phys. Rev. 100 (1955) 545.
[2] J.B. Goodenough, Phys. Rev. 100 (1955) 564.
[3] M. Pissas, G. Kallias, Phys. Rev. B 68 (2003) 134414.
[4] M.T. Fernández-Díaz, J.L. Martínez, J.M. Alonso, E. Herrero, Phys. Rev. B 59 (1999) 1277.
[5] P.G. Radaelli, D.E. Cox, L. Capogna, S.-W. Cheong, M. Marezio, Phys. Rev. B 59 (1999) 14440.
[6] M.R. Ibarra, J.M. De Teresa, J. Blasco, P.A. Algarabel, C. Marquina, J. García, J. Stankiewicz, C. Ritter, Phys. Rev. B 56 (1997) 8252.
[7] A.P. Ramirez, P. Schiffer, S.-W. Cheong, C.H. Chen, W. Bao, T.T.M. Palstra, P. L. Gammel, D.J. Bishop, B. Zegarski, Phys. Rev. Lett. 76 (1996) 3188.
[8] R. Wang, J. Gui, Y. Zhu, A.R. Moodenbaugh, Phys. Rev. B 61 (2000) 11946.
[9] J. Rodríguez–Carvajal, Physica B 192 (1993) 55.
[10] E.F. Bertaut, Acta Cryst. A 24 (1968) 217.
[11] J. Rodriguez-Carvajal, BASIREPS: a program for calculating irreducible representations of space groups and basis functions for axial and polar vector properties. Part of the FullProf Suite of programs, 2007 available at http://www.ill.eu/sites/fullprof/.
[12] C. Ritter, Solid State Phenom. 170 (2011) 263.
[13] A.S. Wills, Physica B 680 (2000).
[14] J.I. Langford, D. Louer, E.J. Sonneveld, J.W. Visser, Powder Diffr. 1 (1986) 211.
[15] N.E. Brese, M. O'Keeffe, Acta Cryst. B47 (1991) 192.
[16] G.H. Rao, K. Bärner, I.D. Brown, J. Phys.: Condens. Matter 10 (1998) L757.
[17] L. Vočadlo, K.S. Knight, G.D. Price, I.G. Wood, Phys. Chem. Miner. 29 (2002) 132.
[18] J.-S. Zhou, J.B. Goodenough, Phys. Rev. B 68 (2003) 054403.
[19] B.F. Woodfield, M.L. Wilson, J.M. Byers, Phys. Rev. Lett. 18 (1997) 3201.
[20] J.J. Hamilton, E.L. Keatley, H.L. Ju, A.K. Raychaudhuri, V.N. Smolyaninova, R. L. Greene, Phys. Rev. B 54 (1996) 14926.
[21] D. Orobengoa, C. Capillas, M.I. Aroyo, J.M. Perez-Mato, J. Appl. Cryst. 42 (2009) 820.
[22] J.C. Toledano, P. Toledano, The Landau theory of phase transitions, World Sci. Lect. Notes Phys. 3 (1987).
[23] M.S. Senn, J.P. Wright, J. Cumby, J.P. Attfield, Phys. Rev. B 93 (2015) 024104.
[24] A. Martinelli, M. Ferretti, C. Castellano, M.R. Cimberle, R. Masini, D. Peddis, C. Ritter, J. Phys, Condens. Matter 25 (2013) 176003.